Master of Science Thesis

Spring 2016

# MRI-BASED QUANTIFICATION OF MAGNETIC SUSCEPTIBILITY

## Assessment of measurement and calculation accuracy


Emma Olsson

Supervisors:
Emelie Lind
Ronnie Wirestam



LUND UNIVERSITY


Department of Medical Radiation Physics
Faculty of Science
Lund University

# Abstract

An object in an external magnetic field will be magnetized and the degree of magnetization is dependent of the magnetic susceptibility of the object. The local magnetic field inside and around an object in the MR scanner will change due to the magnetization of the object. The phase shift is proportional to the local magnetic field, which means that phase images hold information about the susceptibility distribution. Since the magnetic susceptibility is a material property, it will have a specific value for a certain substance. Different tissues and compartment of the brain show different susceptibilities, which makes it possible to use susceptibility as a source of contrast in MRI.

The magnetic field can be described as a convolution of the susceptibility distribution with a dipole field. The susceptibility distribution cannot easily be resolved from this relationship because of the angular dependence of the dipole field. When the dipole field is zero, at the magic angle, the magnetic field will be zero independently of the susceptibility. In Quantitative Susceptibility Mapping (QSM), the susceptibility is calculated through an iterative process comparing the field calculated from an estimated susceptibility distribution to the measured phase.

In this master's thesis, a procedure for QSM has been tested to investigate which conditions and parameters are important for the accuracy of the method. For this purpose, three phantoms were constructed with cylinders of varying susceptibility and geometry. Experiments were made with varying measurement and calculation parameters, and the results were compared to simulated and analytically calculated data.

The results show that the susceptibility images differ substantially in contrast from the original phase images. The method seems to be quite stable for changes in measurement and calculation parameters and it provides an expected linear relationship between estimated susceptibility and concentration of contrast agent. The method does not, however, always retrieve accurate values of the susceptibility for cylindrical objects at an angle about or larger than the magic angle, relative to the main magnetic field. The results seem to be more accurate for large objects or high spatial resolution, large volume coverage and with the slice direction applied along the long axis of the cylindrical object of interest.

# Magnetisk susceptibilitet; en källa till kontrast i MR-bilder

Ett objekt som placeras i det starka magnetfältet i en MR-kamera kommer att bli magnetiserat. Magnetiseringen beskrivs av materialets magnetiska susceptibilitet. Olika delar av hjärnan har olika susceptibilitet vilket gör det möjligt att använda susceptibilitet som en källa till kontrast i MR-bilder. Susceptibiliteten i hjärnan varierar inte enbart med olika vävnader och strukturer utan också med t.ex. syremättnad i blod, venöst blod har högre susceptibilitet än arteriellt blod. Susceptibiliteten hos blod efter en intrakranial blödning kommer att öka med tiden.

Susceptibiliteten ökar också med inlagring av järn i celler. Detta kan ses i flera neurodegenerativa sjukdomar som t.ex. Multipel Skleros (MS) och Alzheimers och Parkinsons sjukdom. Att kunna mäta susceptibilitet i hjärnans olika delar är därför av intresse vid studier av dessa tillstånd. Att kvantitativt kunna mäta susceptibiliteten kan också vara användbart för bestämning av kontrastmedelskoncentration t.ex. vid perfusionsmätningar.

Susceptibiliteten kan inte mätas direkt med MR men fasbilder innehåller information om magnetiseringen och därmed susceptibiliteten. *Quantitative Susceptibility Mapping* (QSM) är en metod för att beräkna susceptibilitet utifrån fasbilder genom en iterativ process.

I ett projekt under våren 2016 har denna metod testats genom mätningar på fantom med känd susceptibilitet. Syftet med projektet var att se hur väl metoden fungerar för att bestämma korrekta värden för magnetisk susceptibilitet och vad som påverkar resultatet. Ett antal fantom skapades bestående av cylindrar placerade i en gel, där varje cylinder först fyllts med en lösning innehållande kontrastmedel (för att öka susceptibiliteten).

Fantomens utformning och olika parametrar för mätning och beräkning av susceptibilitet varierades, t.ex. varierades rumsupplösning, snittriktning och cylindrarnas orientering gentemot det externa magnetfältet.

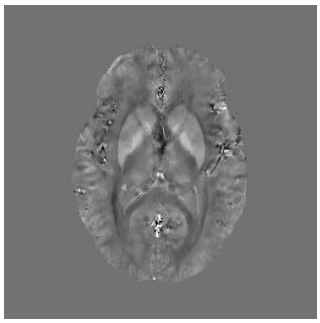

*Susceptibilitetsbilder har en unik kontrast mellan hjärnans olika strukturer.*

Uppmätta värden jämfördes med teoretiska och simulerade värden för fas och susceptibilitet. Metoden visade sig ge värden som stämde bra överens med teorin för cylindrar orienterade parallellt eller nära parallellt med det magnetiska fältet men för vinklar runt, eller större än 54,7 ° (kallat den magiska vinkeln) underskattades susceptibiliteten. Vinkelberoendet var dock mindre tydligt än i de ursprungliga fasbilderna.

Simuleringar visade att vinkelberoendet inte var ett resultat av susceptibilitetsberäkningen utan berodde på en avvikelse i fas utanför cylindrarna i snittriktningen. Detta fel verkade uppkomma redan vid mätningen. Att välja en snittriktning längs cylindern gav bättre resultat för cylindrar orienterade ungefär vinkelrätt mot magnetfältet. En god rumsupplösning eller ett stort objekt visade sig också påverka resultatet positivt.

Susceptibilitetsbilder kan alltså beräknas med gott resultat, men för långsmala objekt, som t.ex. blodkärl, är geometrin av betydelse. Värdena i bilderna är också relativa, för att beräkna kvantitativa värden för susceptibiliteten in vivo hade det behövts någon referens i bilden med känd susceptibilitet

# Table of content

# Introduction

When an object is exposed to an external magnetic field, for example the strong magnetic field of an MR scanner, it will become magnetized and the local magnetic field inside as well as surrounding the object will change. How the object is magnetized depends on a material property called magnetic susceptibility and on geometric factors.

Generally, in magnetic resonance imaging (MRI), magnetic susceptibility is associated with artefacts since large differences in susceptibility between two adjacent materials, e.g. tissue and air, can lead to image distortion and, in gradient echo imaging, signal loss due to shortening of $T_2^*$ [1]. An example of a typical susceptibility artefact is seen in Figure 1. However, since susceptibility is a material property, information about the susceptibility of a certain tissue can also provide valuable information.

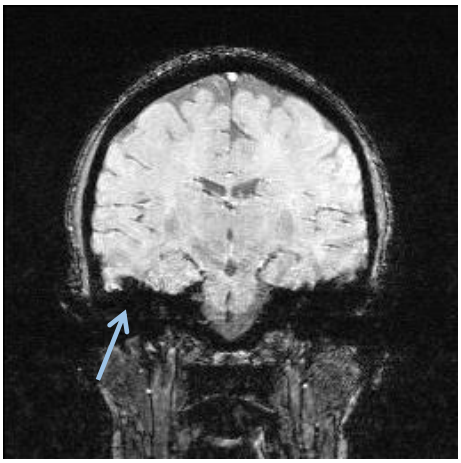

*Figure 1 Signal loss and image distortion in a gradient echo MR image due to differences in susceptibility between air and tissue.*

The magnetic susceptibility differs among tissue types and tissue regions, since the tissue compartments are built up in different ways and by different substances. Therefore, the susceptibility can be used as a source of contrast in MRI. An example of a parametric susceptibility image is presented in Figure 2. No contrast agent has been used to obtain the image, i.e., the contrast originates only from the difference in magnetic susceptibility between different regions. Two examples of regions with widely separated susceptibilities are indicated in the figure. Globus pallidus which is a part of the basal ganglia, has a susceptibility of 0.105 ppm and white matter has a lower susceptibility of -0.030 ppm [2].

Some physiological or pathological conditions can make the properties of tissues change. For example, iron accumulation in inflamed myelin cells, as in a multiple sclerosis (MS) plaque, increases the susceptibility of the myelin [3]. Iron accumulation is also seen in other neurodegenerative diseases, for example, Alzheimer's and Parkinson's diseases [4]. The magnetic susceptibility is also dependent on the oxygen saturation level of blood. The susceptibility increases with increasing levels of deoxyhemoglobin. Venous blood will thus have a higher susceptibility than arterial blood and the susceptibility will change with deoxygenation, for example for extravasated blood from an intracranial haemorrhage. [5] Being able to measure the susceptibility could thus be beneficial in the studies of these conditions.

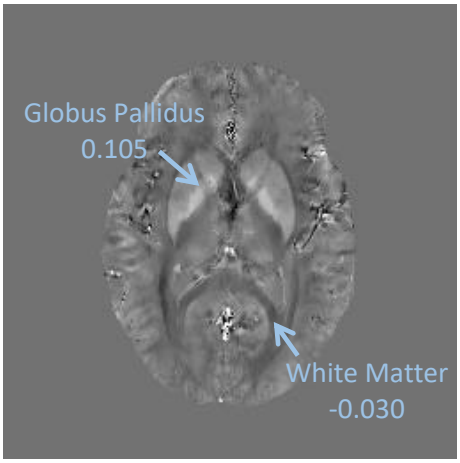


*Figure 2 A susceptibility image (units in ppm) showing a transversal slice of a human brain.*

Quantitative measurements of the susceptibility could also be potentially useful to determine the concentration of contrast agent. The knowledge of contrast agent concentration in vivo could be used for example to improve perfusion measurements using dynamic susceptibility contrast (DSC-MRI) or dynamic contrast enhanced (DCE-MRI) [6].

Unfortunately, it is not possible to measure the magnetic susceptibility directly by MRI, but as the susceptibility affects the magnetic field, and the field change

is proportional to the MR signal phase shift, it is possible to obtain information about susceptibility from MR phase images.

*Quantitative Susceptibility Mapping*, QSM, is a recently proposed method of calculating susceptibility from measured phase data. In this project, the method of QSM has been evaluated in phantoms with known concentrations of gadolinium contrast agent, to establish whether the method can deliver accurate results with respect to quantitative magnetic susceptibility values. The measured phase values and the magnetic susceptibility estimates, calculated by QSM, has been compared to values calculated using theoretical relationships.

Various phantom designs have been employed as well as various parameters and settings in the measurements and in the susceptibility calculation, in order to establish important sources of error and optimal settings to produce an accurate susceptibility map.

Hence, the purpose of this study was to evaluate a common QSM measurement and calculation procedure, to establish which parameters and conditions are the most important in obtaining an accurate quantitative result in magnetic susceptibility mapping.

# Theory

## Magnetic susceptibility and magnetism

Magnetic susceptibility, $\chi$, is a material property which describes how a material becomes magnetized in an external magnetic field. The magnetic susceptibility of a substance is determined by its electron configuration and the associated atomic magnetic dipole field. Atomic electrons are sorted in energy states two and two, with opposite magnetic moments that cancel each other out. In the case of an odd number of electrons there will be an unpaired electron resulting in a non-vanishing magnetic moment. These atoms can be seen as magnetic dipoles with a permanent magnetic dipole moment. The nuclear spin, that is the source of the MR signal, also represents a magnetic moment but this is much smaller than an atomic magnetic moment. The atomic magnetic moment will therefore have the dominate effect on the local magnetic field.

The movement of the electrons around a nucleus can be treated as a current in a closed loop. According to Faradays law of electromagnetic induction a change in magnetic flux in a conducting loop will give rise to a current through the loop directed so that the corresponding magnetic field counteracts the original magnetic field change. In all materials, when exposed to an external magnetic field, an induced dipole moment will therefore arise that counteracts the external field. This effect will only be noticeable in materials without a permanent atomic magnetic dipole moment, and such materials are called diamagnetic. This effect corresponds to a negative magnetic susceptibility, $\chi < 0$.

Normally, in materials with a permanent atomic magnetic dipole moment, the magnetic moments will be randomly orientated and provide no net magnetization. However, in the presence of an external magnetic field, the atomic moments will align and slightly increase the total magnetic field. This is called paramagnetism and corresponds to a positive susceptibility, $\chi > 0$.

Ferromagnetic materials have permanent domains of atomic spin magnetic moments. An external field can make these domains align, and ferromagnetic materials tend to remain magnetized after removal of the external field, a phenomenon exploited in the construction of permanent magnets. The magnetic susceptibility of a ferromagnetic material is high, $\chi \gg 1$.

When an object is placed in an external magnetic field, for example the strong magnetic field of an MR scanner, atomic moments will be affected as described above and will give rise to a magnetization according to

$$M = \chi \cdot H \tag{1}$$

The size of the magnetization vector, $M$, is dependent on the magnetic susceptibility, $\chi$, of the object and the magnetic field strength, $H$, of the external magnetic field. Because of the magnetization of the material the local magnetic field inside and around the object will change. The magnetic flux density, $B$, is given by

$$B = \mu_0(\chi + 1)H \tag{2}$$

where $\mu_0$ is the magnetic permeability of free space.

## The dipole field

Every magnetic dipole is surrounded by a magnetic field. The magnetic field, $B$, at a distance $r$ along an angle $\theta$, relative to the direction of the dipole, caused by a magnetic dipole with magnetic moment $m$ can be described as

$$B \propto \frac{m}{r^3}(3\,cos^2\,\theta - 1) \tag{3}$$

This means that the magnetic field shows an angular dependence around a spin. Figure 3 shows the magnetic field around a magnetic dipole in two dimensions. The angle at which the term $(3\cos^2\theta - 1)$ equals zero is called the magic angle and is approximately 54.7 °. At the magic angle, the magnetic field will be zero independently of the size of the magnetic moment.

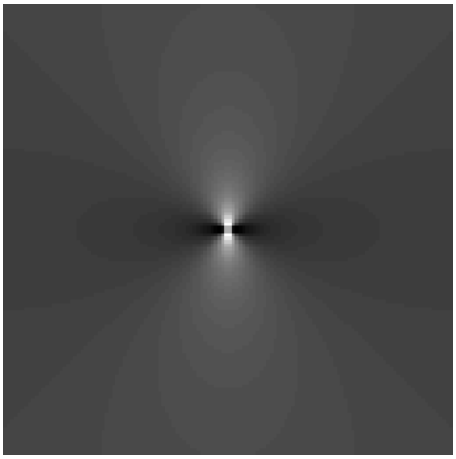

*Figure 3 The magnetic dipole field in two dimensions.*

## Phase images

The complex MR signal can be described as a vector (or a complex number) with a magnitude and an angle as illustrated in Figure 4. The magnitude can be calculated as the absolute value of the signal $Mag = \sqrt{Im^2 + Re^2}$ and the phase is calculated by $\phi = \arctan\frac{Im}{Re}$, where $Re$ and $Im$ are the real and imaginary parts, respectively. MR images are usually built up by the magnitude of the signal but images can also be constructed from the phase data (as further described in the following section).

Phase angles larger than $2\pi$ cannot be distinguished from the $2\pi$ lower phase since the angle will appear to be the same. Phase shifts larger than $2\pi$ will therefore lead to wraps, or aliasing, in the phase image.

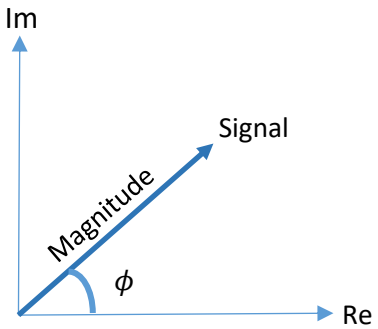


*Figure 4 Illustration of the complex MR signal*

## Phase shift and magnetic field

The MRI angular precession frequency $\omega$ is dependent on the magnetic field according to the Larmor equation

$$\omega = \gamma \cdot B\,, \tag{4}$$

where $\gamma$ is the gyromagnetic constant. Variations in the local magnetic field, with position $r$, will therefore lead to differences in frequency. At the time of the signal acquisition differences in precession frequency will correspond to phase-shift variations, and the phase evolution $\phi(r)$ will also depend on the echo time, $TE$.

$$\phi(r) = \omega(r) \cdot TE = \gamma \cdot B(r) \cdot\ TE \tag{5}$$

Note that, for longer TEs, the phase angles will be generally larger and the risk for aliasing increases. In order for the phase images to be useful there is a need for a method for unwrapping as well as for filtering of background field variations. The unwrapping can be accomplished by a region growing algorithm which finds gradients that corresponds to a difference by a multiple of $2\pi$ and adding or subtracting $2\pi$ [7]. Filtering is needed since in the unwrapped image there is usually a remaining background phase gradient over the entire image. This phase does not arise from the susceptibility distribution inside the object but from, for example, imperfect shimming or susceptibility sources outside the imaging volume. *Projection onto Dipole Fields* (PDF) [8-9] is one method for background field removal that compares magnetic fields generated from magnetic dipoles inside and outside a region of interest. Other examples of filtering methods are *Laplacian Boundary Value* (LBV) [10] and *Regularization Enabled Sophisticated Harmonic Artefact Reduction for Phase data* (RESHARP) [11].

In accordance with the Maxwell equations, the induced phase shift will be dependent on the magnetic susceptibility of an object as well as on the orientation of the object relative to the main magnetic field. For elongated objects, for example, cylinders, the angular dependence is very distinct. Figure 5 shows a phase image of an object with cylinders with the same susceptibility but oriented in different directions relative to the main magnetic field $B_0$. For the cylinder oriented parallel to the field the phase shift is positive and for the cylinder oriented perpendicular to the field the phase shift is negative.

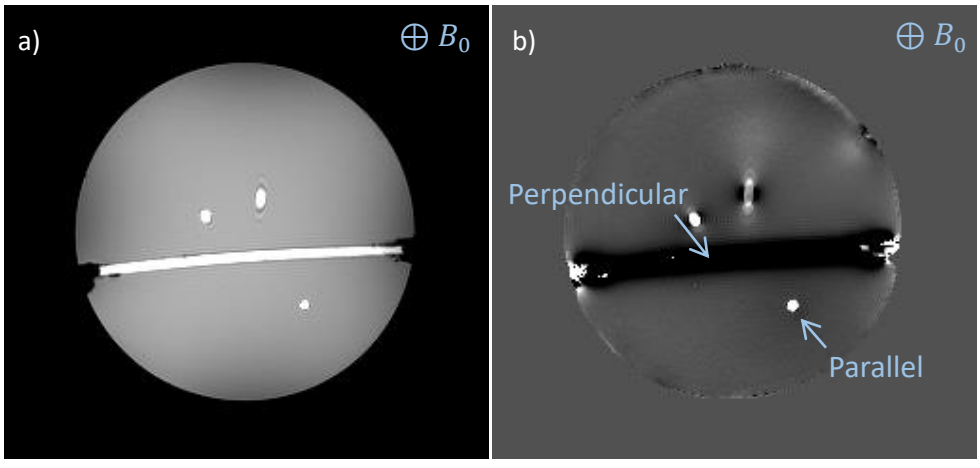


*Figure 5 The magnitude image (a) and the phase image (b) of an object with cylinders orientated at different angles relative to the main magnetic field $B_0$. The phase is positive for the parallel cylinder and negative for the perpendicular cylinder.*

## Magnetic field in cylinders

For cylinders, the magnetic field change due to the susceptibility difference between cylinder and the background can be calculated analytically. The internal and external fields corresponding to an infinitely long cylinder are given by

$$\Delta B_{in} = \frac{\Delta\chi}{6}(3\cos^2\theta - 1)B_0 + \frac{1}{3}\chi_{ex}B_0 \quad (6)$$

$$\Delta B_{ex} = \frac{\Delta\chi}{2}\frac{a^2}{\rho^2}\sin^2\theta\cos 2\varphi\, B_0 + \frac{1}{3}\chi_{ex}B_0 \quad (7)$$

where $\Delta\chi = \chi_{\text{in}} - \chi_{\text{ex}}$ , i.e., the difference in susceptibility between the inside and the outside of the cylinder, $a$ is the radius of the cylinder, $\theta$ is the angle between the direction of the $B_0$-field and the cylinder axis and $\rho$ and $\varphi$ are the cylindrical coordinates describing a point at distance $\rho$ and at an angle $\varphi$ relative to a point at the centre of the cylinder [1].

## Magnetic susceptibility and magnetic field

For more complicated geometries, the relationship between the field perturbation and the susceptibility cannot be described as easily as for cylinders. However, more generally, the local field change due to the introduction of an object in the field can be described as a convolution of a dipole field kernel and the susceptibility distribution,

$$\Delta B(r) = \frac{3\cos^2\theta - 1}{4\pi r^3} \otimes \chi(r) \quad (8)$$

where $r$ and $\theta$ are spherical coordinates and $\chi$ denotes the magnetic susceptibility [12]. Combining this with equation 5 gives the relationship between phase and susceptibility

$$\Delta\phi(r) = \gamma \cdot TE \cdot \frac{3\cos^2\theta - 1}{4\pi r^3} \otimes \chi(r) \quad (9)$$

The main idea of QSM is to extract the susceptibility distribution from Equation 9 using the information of the local magnetic field from the phase image. However, the susceptibility distribution cannot easily be resolved from this equation. The problem arises when the dipole kernel approaches zero at the magic angle. A convolution in real space represents a multiplication in k-space, and extracting the susceptibility distribution from Equation 8 by deconvolution would therefore imply a division by zero at some coordinates in k-space which would, in principle, affect every point of the $\chi(r)$ solution in real space. This is why the task, to calculate susceptibility from the phase, is usually referred to as an ill-posed inverse problem.

## MEDI

*Morphology Enabled Dipole Inversion* (MEDI) [9, 12-14] is a QSM method, designed to solve the ill-posed inverse problem of resolving $\chi(r)$ according to Equation 8. In the MEDI approach the problem is formulated so that the difference between an estimated field map and the measured field map should be of the order of the noise level $\varepsilon$. This can be written as

$$\|W(\delta - FT^{-1}(D \cdot FT(\chi)))\|_2 \leq \varepsilon \quad (10)$$

where $W$ is a weighting matrix, $\delta$ is the measured field and $D$ is the dipole field in k-space.

MEDI also uses the fact that changes in susceptibility follows the morphological boundaries and that the susceptibility map therefore should have gradients in the same locations as the magnitude image. The problem can then be written as

$$min_{\chi}\|M\,\nabla\chi\|_1 \; subject\; to\; \|W(\delta - FT^{-1}(D \cdot FT(\chi)))\|_2 \leq \varepsilon \qquad (11)$$

where $M$ is a matrix that has the value 0 where there is a gradient in the magnitude image and 1 otherwise. By adding the first term of equation 11, the susceptibility is estimated so that gradients in the estimated susceptibility map corresponds to gradients in the magnitude image [12].

The problem of Equation 11 is solved through an iterative process. An initial guess is made for the susceptibility distribution. Convolving this with the dipole kernel gives an estimated field map. The estimated field map is compared to the measured field map, i.e. the phase image, and the difference, the error, is used to update the initial guess. The updated susceptibility distribution is then used as input when this procedure is repeated. Iterations are made until the result fulfils the requirements. This iterative process is illustrated in Figure 6.

The $l_1$and $l_2$norms constitute measures of the length of a vector and in the same way the magnitude of a matrix. The $l_p$-norm is defined as

$$\|x\|_p = \sqrt[p]{\sum_i |x|_i^p} \qquad (6)$$

where $x$ is an arbitrary vector or matrix, $p$ is a positive integer and $i$ denotes the elements of $x$.

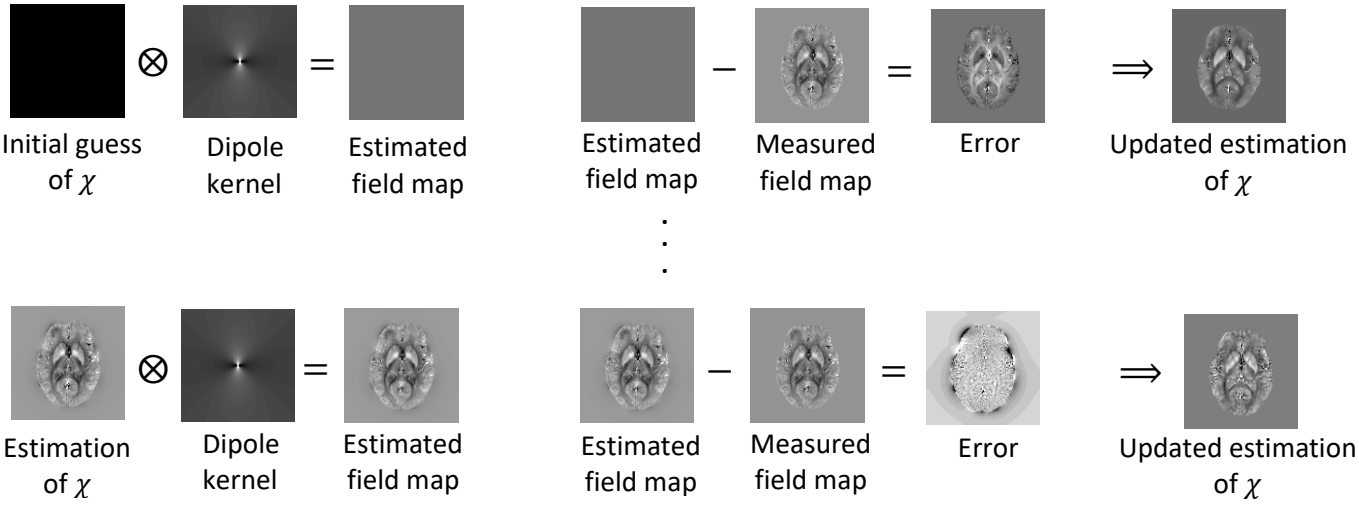


*Figure 6 Illustration of the iterative process in MEDI. An initial guess is made for the estimated susceptibility and convolved with the dipole kernel to create an estimated field map. This is compared to the measured field map and the estimated susceptibility distribution is updated. These steps are repeated until the difference between the estimated and measured field map is small enough.*

## The regularization parameter $\lambda$

The Lagrange multiplier method is used to rewrite the problem in Equation 11 as a minimization of a cost function [12]

$$E(\chi,\lambda) \equiv \|M\,\nabla\chi\|_1 + \lambda\left(\left\|W\left(\delta - FT^{-1}(D \cdot FT(\chi))\right)\right\|_2 - \varepsilon\right) \qquad (7)$$

The value of the regularization parameter, $\lambda$, determines how much the information from the magnitude image versus the phase image is prioritized.

# Method

## Phantom design

In order to evaluate the QSM method with respect to phase measurement as well as mathematical reconstruction, three different phantoms were constructed. Cylinders of thin plastic were filled with a paramagnetic gadolinium (Gd) contrast agent solution (DOTAREM, Guerbet), sealed and glued on the inside of a container. The container with cylinders was subsequently filled with agarose gel doped with a small amount of nickel in the form of nickeldinitridhexasulphate ($\mathrm{Ni(NO_3)_2(H_2O)_6}$). The gel was designed according to a locally developed preparation routine using 1 % agarose and 0.24 mM nickel [15]. The susceptibility of the gel was calculated through Wiedemann's additivity law for the susceptibility of mixtures: $\chi = p_1\chi_1 + p_2\chi_2 + \cdots p_n\chi_n$ where $p_n$ is the concentration of substance $n$ [16, 17].

The purpose of the contrast agent was to obtain a controlled increase of the susceptibility inside the cylinders to achieve a difference in susceptibility between the cylinders and the background resembling different compartments in the human body.

The theoretical values used for the susceptibility of water, nickel and gadolinium are presented in Table 1. The calculated values for the gel and the 0.5 mM gadolinium solution are also included.

*Table 1 The magnetic susceptibility of the different components of the phantoms.*

| | |
|---|---|
| $\boldsymbol{\chi(\mathrm{water})}$ | -9.022 ppm [17] |
| $\boldsymbol{\chi_{\mathrm{mol}}(\mathrm{Ni(NO_3)_2(H_2O)_6})}$ | 54 ppm $\mathrm{M}^{-1}$ [18] |
| $\boldsymbol{\chi_{\mathrm{mol}}(\mathrm{Gd})}$ | 326 ppm $\mathrm{M}^{-1}$ in reference to water [19] |
| $\boldsymbol{\chi(\mathrm{gel})}$ | -9.017 ppm |
| $\boldsymbol{\chi(0.5\ \mathrm{mM\ Gd})}$ | -8.859 ppm |

In the first phantom design, cylinders with 5 mm diameter, filled with 0.5 mM Gd solution, were positioned at five different angles relative to the main magnetic field (approximately 0, 30, 55, 75 and 90°). The actual angles were measured in the resulting images.

The second phantom design consisted of 5 mm diameter cylinders with varying concentration of Gd contrast agent. The concentrations used were 0, 0.2, 0.4, 0.6, 0.8, 1, 2, 4, 6, 8 and 10 mM. In the third phantom cylinders containing 0.5 mM Gd solution with a diameter of 2, 2.6, 4.7, 5, 7.4, 9 and 10.8 mm were used. The three phantom designs are shown in Figure 7.

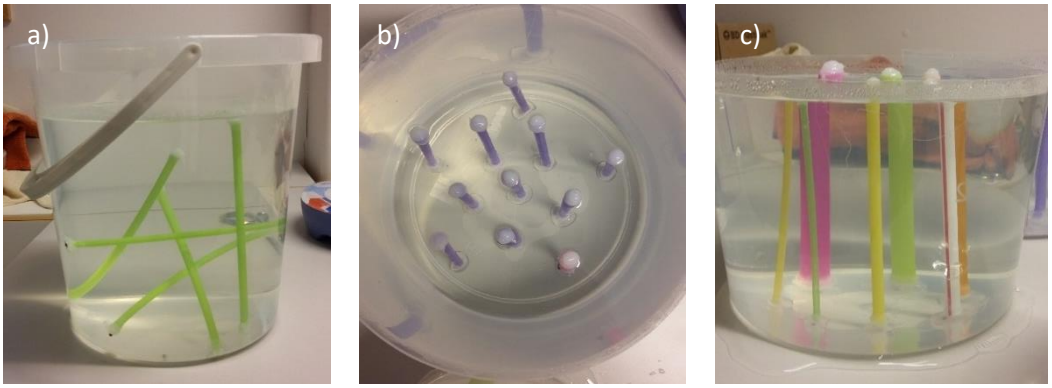


*Figure 7 Photographs of the three different phantoms with a) cylinders oriented at different angles, b) varying concentrations of contrast agent and c) cylinders of different diameters.*

## Measurements

Measurements were carried out on a 3T MRI scanner (MAGNETOM Trio, Siemens) using an imaging protocol according to Table 2. The parameters were selected according to the recommendations for QSM of human brain given by the Cornell MRI research lab [20].

A multi-TE gradient echo sequence was used since a single acquisition is not sufficient for deriving the magnetic field from the phase, due to an offset in the magnetic field depending on the conductivity of the material. At the measurement, the MRI scanner sets the Larmor frequency, representing the frequency that will be set to zero in the rotating frame of reference, and thus the measured phase shift will be relative to this reference, which in this case will be in the background gel.

*Table 2 Imaging parameters in the standard protocol used for QSM phase measurements.*

| | |
|---|---|
| **Sequence** | 3D Multi-TE Gradient Echo |
| **Number of echoes** | 11 |
| **Echo spacing, ΔTE** | 6.78 ms |
| **Flip angle** | 20 ° |
| **Band width** | 150 Hz/pixel |
| **Field of view, FOV** | 24 cm |
| **Slice thickness** | 2 mm |
| **Number of averages** | 1 |
| **Matrix size** | 256 x 240 |

In the evaluation process, this protocol was subsequently altered to accomplish measurements with isotropic voxels, different spatial resolutions and shorter TE. The different parameter changes are described below.

### Spatial resolution

Measurements were performed with varying spatial resolution (altered matrix size and fixed volume of interest). A FOV of 205x205 mm and an excited slab of 32 mm was used. The matrix sizes used were 64x64, 128x128, 256x256 and 512x512, corresponding to isotropic voxels with sides 0.4, 0.8, 1.6 and 3.2 mm, respectively.

### Volume coverage

Measurements in which only the number of slices was varied were carried out, implying varied volume of interest. The voxel size was 0.8x0.8x0.8 $mm^3$ and the number of slices was 40, 60, 104 and 144.

## Image processing and QSM calculation

For post-processing of the measured images, a MEDI MATLAB code package for QSM, from Cornell MRI Research Lab [20], was used.

A set of magnitude and phase images, one for each echo time, were obtained from the MRI scanner. These were combined to one magnitude and one phase image stack. The phase images were then unwrapped [7] and subsequently filtered with the PDF approach [8-9]. The phase images were also masked before it was supplied to the MEDI algorithm. The mask was created using a threshold-based approach on information from the magnitude image to define the region corresponding to the object. The mask determines which volume to include in the susceptibility calculation. Examples of images from the MR scanner, as well as the combined, unwrapped, filtered and masked phase image are shown in Figure 8.

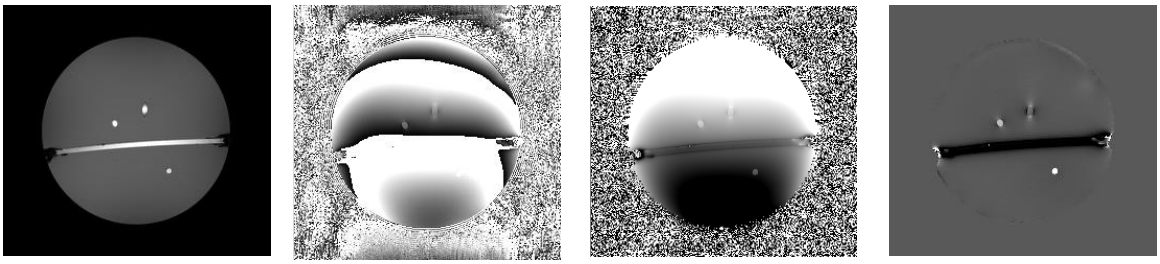

Magnitude | Phase | Combined phase image, unwrapped | Filtered and masked phase image

*Figure 8 An example of a magnitude and a phase image from the MR scanner, and the combined phase image after unwrapping, filtering and masking.*

## Variations in post processing and QSM calculation

### Masking

Edge slices of the phase image stack were removed in the mask and the effect on the susceptibility images of this removal was evaluated.

### Filtration method

A few different methods for phase background removal were compared, i.e., *Projection onto Dipole Fields (PDF)* [8-9], *Laplacian Boundary Value (LBV)* [10], and *Regularization Enabled Sophisticated Harmonic Artefact Reduction for Phase data, (RESHARP)* [11] for filtering of the measured phase images.

### Variation of $\lambda$

The susceptibility images were calculated using $\lambda$ settings 1, 10, 100, 1000, 10 000 and 50 000.

### Zero padding

Zero padding was performed in the spatial room by padding the matrix symmetrically with 200 zeros in all three dimensions. The purpose of the zero padding was to improve the image quality by a narrower spacing of data points in k-space, giving the appearance of more data points.

### Simulation

A simulated phase image was constructed by creating a template from the magnitude image that distinguishes between cylinders and gel. Artificial susceptibility images were then created by assigning the theoretical values of the susceptibility for agarose gel or gadolinium solution to the respective pixels. From the artificial susceptibility image, a simulated phase image was calculated using Equation 9. This simulated phase image was then used as input to the MEDI algorithm and simulated QSM maps were obtained. The construction of the simulated phase image is illustrated in Figure 9.

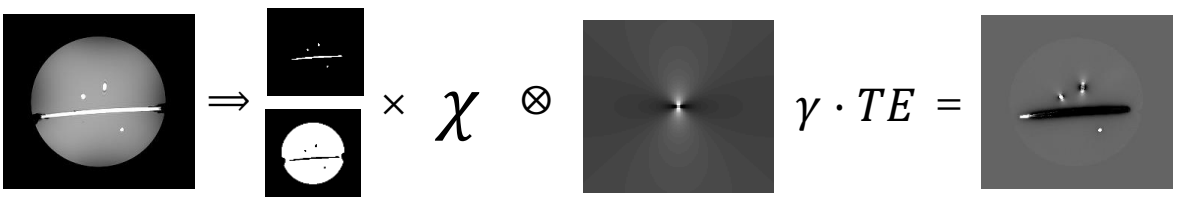


Magnitude image | Template | Theoretical susceptibility | Dipole field | Constants | Simulated phase image

*Figure 9 Illustration of the construction of a simulated phase image.*

### Image analysis

Experimental as well as simulated phase and QSM images were evaluated by measuring the value of interest in ROIs placed in the cylinders, and experimental values were compared with the corresponding theoretical and/or simulated values.

### In vivo measurement

To show an example of QSM in vivo, sagittal brain images were obtained from a healthy volunteer, using the same imaging protocol and calculation procedure as for the phantom measurements in order to visualize differences between phase and QSM data in the human brain. The volunteer gave informed consent before participation.

## Results

### Phantoms

#### Cylinder angle

Figure 10 shows a phase image and a corresponding susceptibility image of the phantom with cylinders of varying angles. So-called blooming effects in the phase image, related to the properties of a dipole field, are seen around cylinders not oriented parallel to the main magnetic field. Some unwanted residues of this blooming effect can be seen in the susceptibility image.

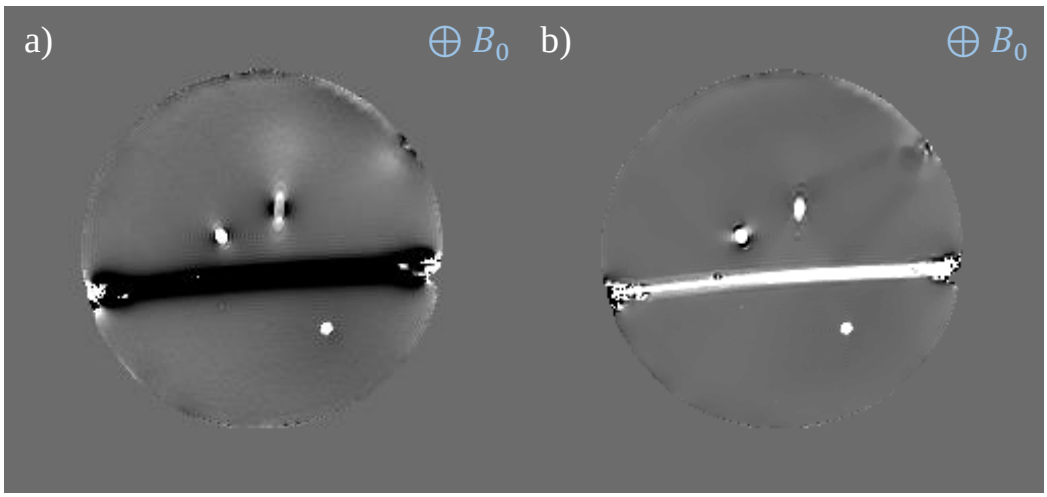


*Figure10 Phase image (a) and the corresponding calculated susceptibility image (b) of the phantom with varying angles of the cylinders (slice 17 of 48).*

In Figure 11, the numerical results from the measurement with cylinders at different angles are presented as well as the corresponding analytically calculated values. The phase inside the cylinders corresponded well with the theoretical values, but the susceptibility deviated considerably for angles larger than the magic angle.

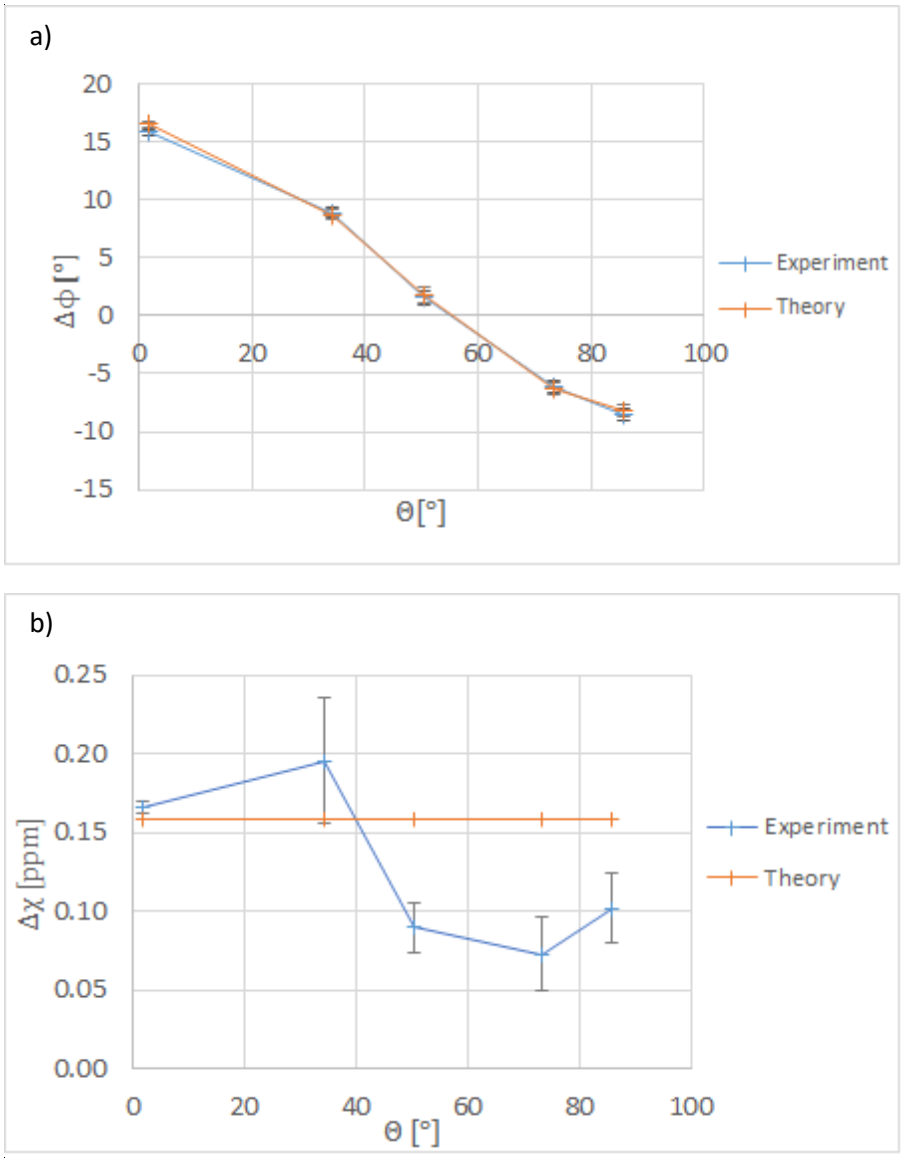


*Figure 11 Experimental and theoretical values of (a) phase and (b) susceptibility inside the cylinders oriented at different angles relative to the main magnetic field. The standard deviation within the region of interest is presented as error bars for the experimental data.*

## Concentration of gadolinium solution

Figure 12 displays the corresponding phase and susceptibility images for the phantom with cylinders with different concentrations of gadolinium. As can be seen in figure 13, for low concentrations, the measured phase and susceptibility values correspond well with the theoretical values. The difference between experiment and theory increased at higher concentrations of gadolinium. The expected linear dependences of both phase and susceptibility on the concentration of gadolinium can be seen, although problems with insufficient phase unwrapping occurred at high concentrations. For the phase data, this was compensated for manually by simply adding $2\pi$ to the observed values. It was, however, not possible to evaluate the susceptibility data for concentrations above 4 mM.

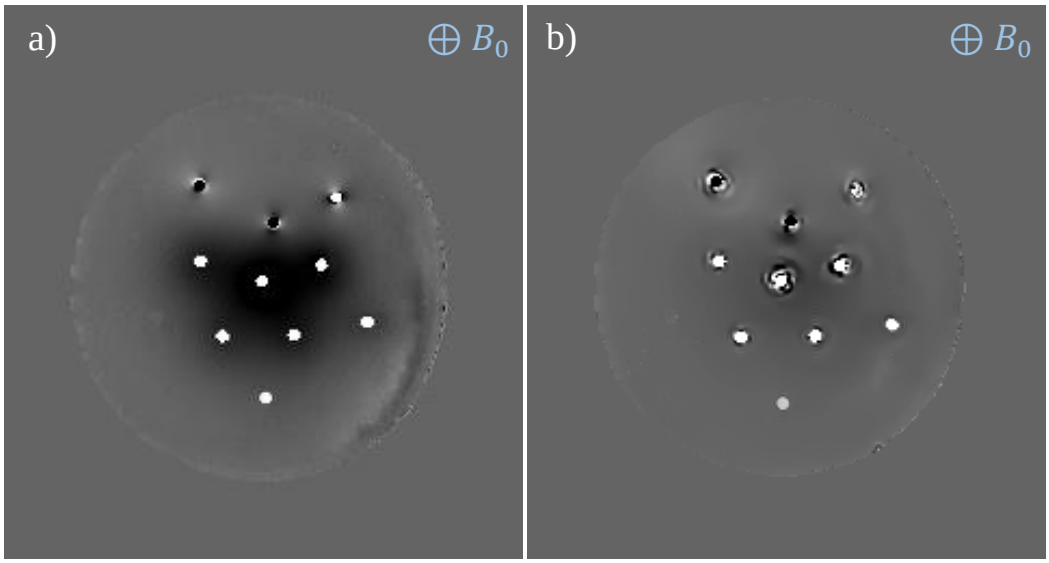


*Figure 12 The (a) phase image and (b) susceptibility image of a middle slice of the phantom with concentrations of gadolinium from 0 to 10 mM. Cylinders with the highest concentrations are at the top of the images.*

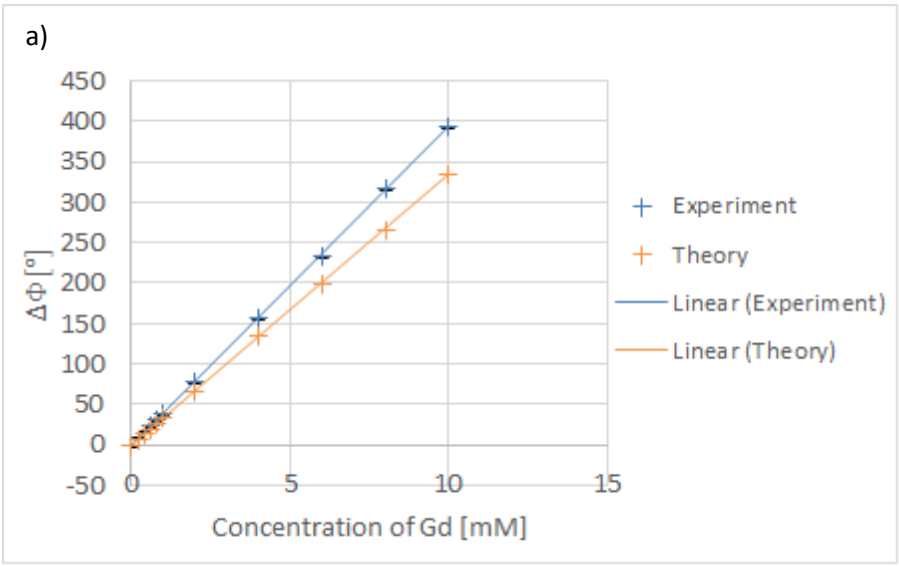

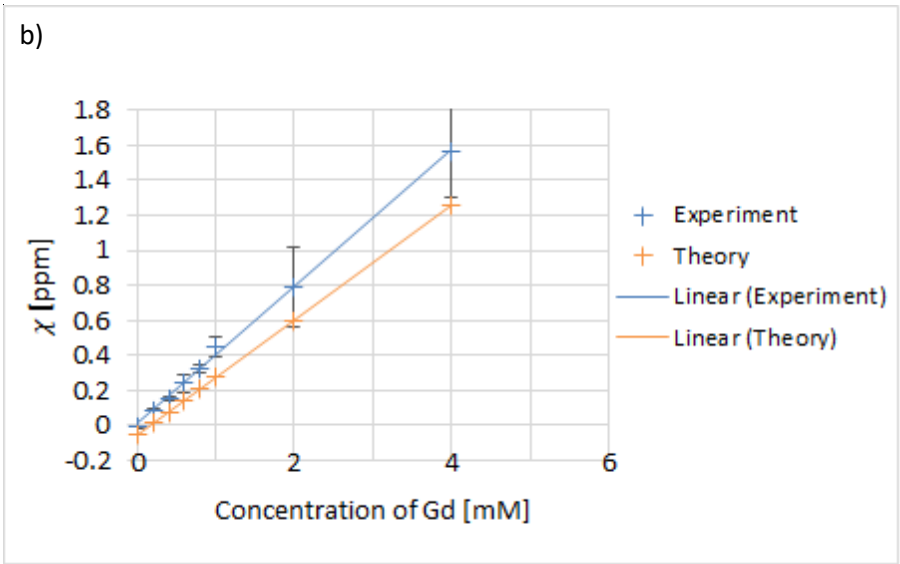


*Figure 13 (a) Phase and (b) magnetic susceptibility as a function of the concentration of gadolinium contrast agent. For the three highest concentrations in (a), the phase was manually unwrapped. The standard deviation within the region of interest is presented as error bars for the experimental data.*

## Cylinder diameter

The image results of the measurement with cylinders of varying diameters, orientated perpendicular to the main magnetic field, are presented in Figure 14. Quantitative susceptibility estimates for the seven cylinders, at parallel and perpendicular orientations, are presented in Figure 15. The result for the 5 mm cylinder can be compared with the results in Fig. 11 b) (for 0 and 90 degrees), and approximately the same susceptibility estimates were obtained in the two different phantoms.

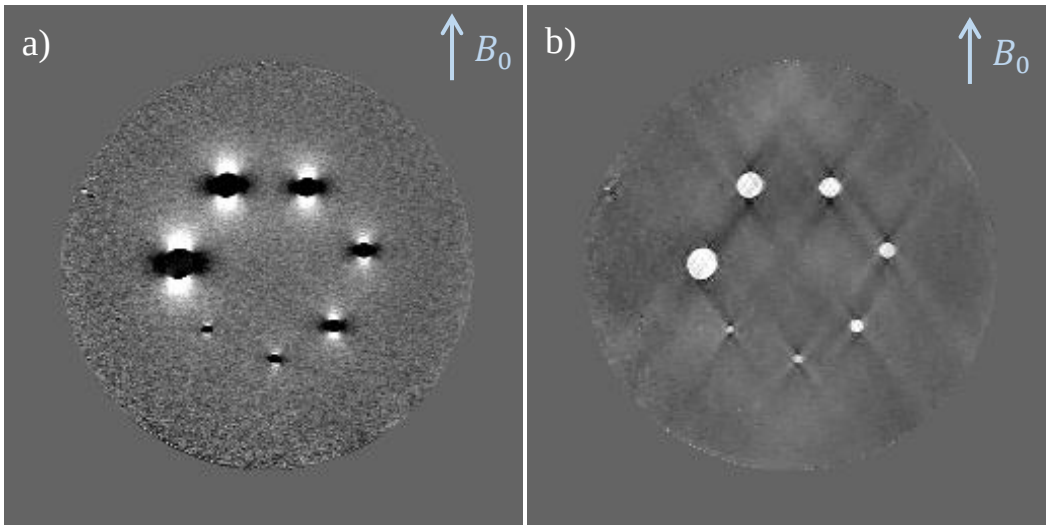


*Figure 14 (a) The phase image and (b) the susceptibility image of a middle slice of the phantom with different cylinder diameters. The images shown are from a measurement done with the cylinders orientated perpendicular to the field.*

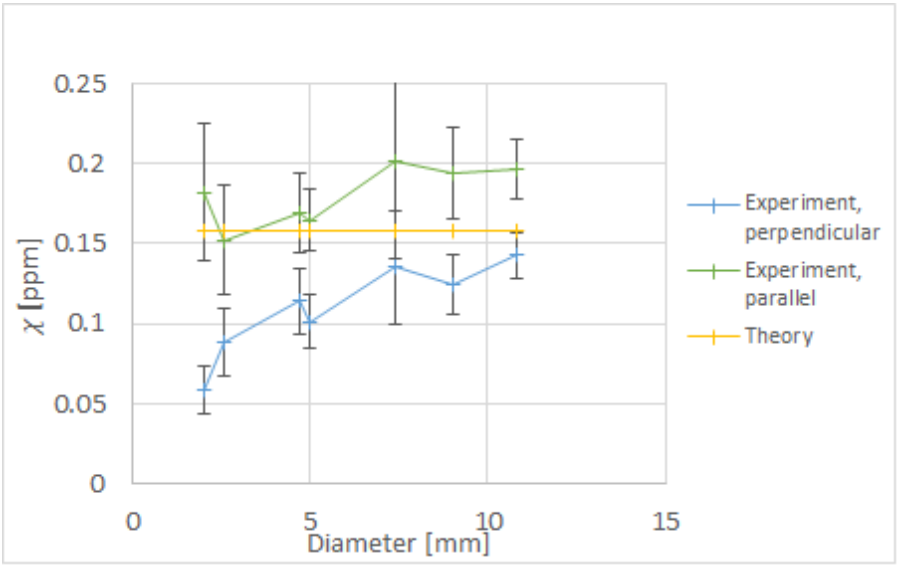


*Figure 15 Measured susceptibility as a function of cylinder diameter. Results for cylinders parallel and perpendicular to the main magnetic field are compared with the theoretical value. The standard deviation within the region of interest is presented as error bars for the experimental data.*

## Variation of measurement parameters

### Spatial resolution

The phantom with different diameters was measured, with the cylinders orientated perpendicular to the main magnetic field, at different spatial resolutions. The susceptibilities in the 5 mm and 10.8 mm cylinders are presented as a function of pixel size in Figure 16.

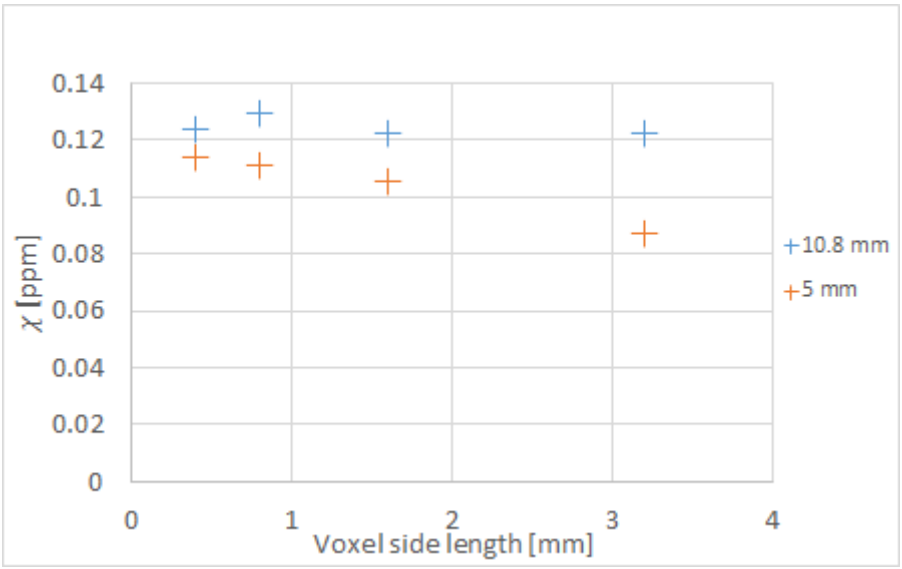


*Figure 16 Susceptibility estimates in the centre of the 10.8 mm and the 5 mm perpendicularly oriented cylinders, for different isotropic spatial resolutions.*

### Volume coverage

Figure 17 shows the result of measuring with different volume coverage. The same slice thickness (0.8 mm) was used for each acquisition.

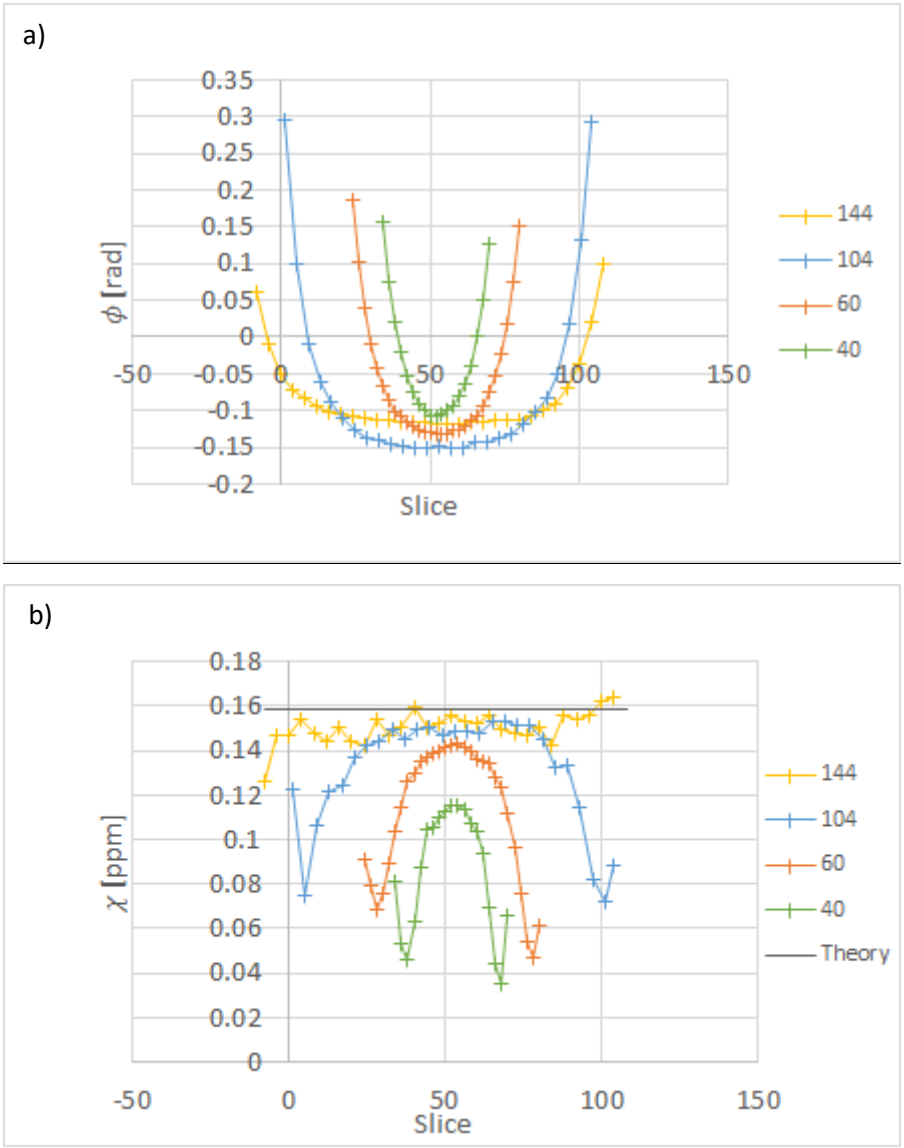


*Figure 17 The diagrams show (a) the phase and (b) the susceptibility, measured in the largest cylinder of the diameter phantom for a varying number of slices.*

## Variations in the QSM calculation

### Masking

When the edge slices of the phase image stack were removed before input to the MEDI algorithm, artefacts were reduced in the final QSM image. This was particularly obvious when an older version of the MEDI software was employed due to the use of central difference for the discrete calculation of the gradient and the divergence of the magnitude and susceptibility image. The updated version used forward and backward differences to calculate gradient and divergence, and this seemed to provide images with fewer artefacts.

Susceptibility images calculated with and without the edge slices are shown in Figure 18. Figure 19 shows a profile through the largest cylinder, in the slice direction, with and without edge slices.

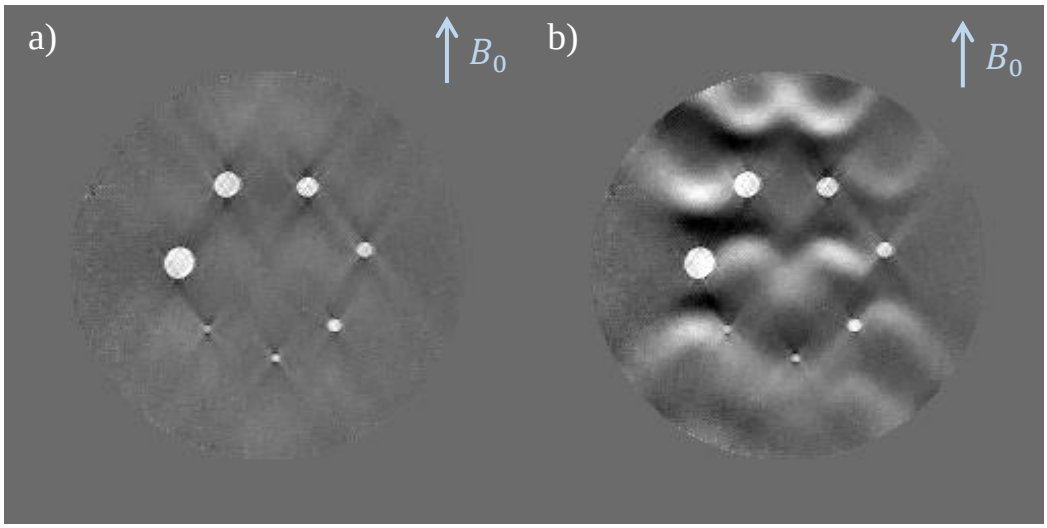


*Figure 18 Middle slice of susceptibility images calculated for the diameter phantom with central differences (a) without and (b) with the first and last three slices of the phase image stack.*

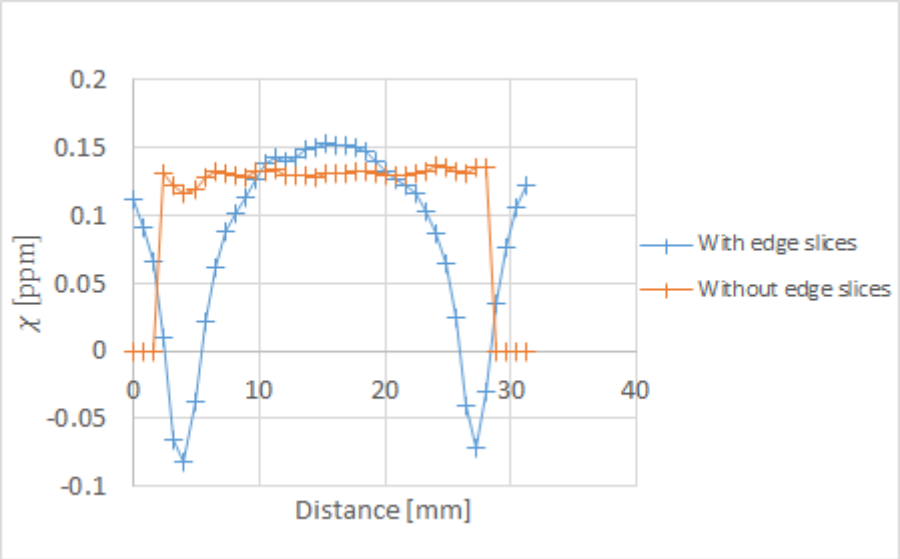


*Figure 19 QSM profile inside the largest cylinder throughout the slice direction, with and without inclusion of the edge slices*

## Filtering methods

Susceptibility estimates obtained using phase data filtered with three different methods for background field removal (PDF, LBV and RESHARP) and without any filtering method are presented in Figure 20.

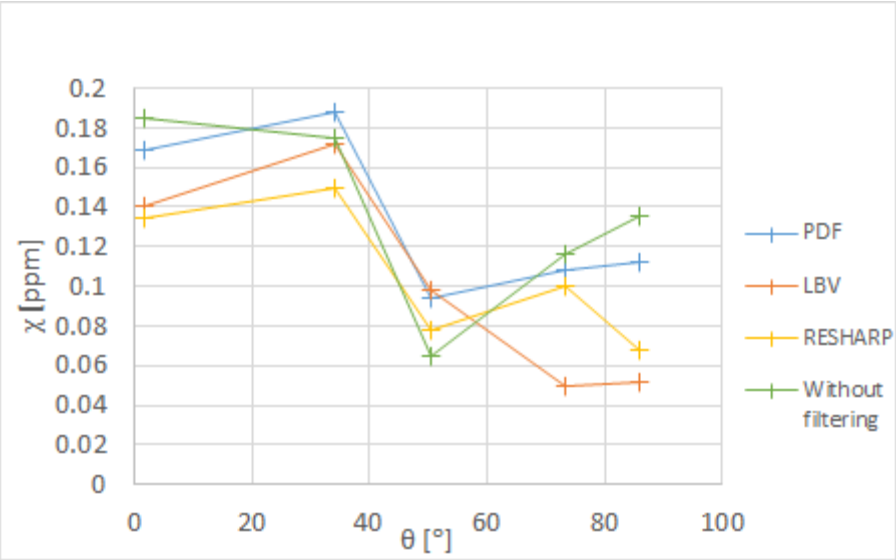


*Figure 20 Susceptibility in cylinders orientated at different angles relative to the main magnetic field, calculated using three different filtering methods (PDF, LBV and RESHARP) and without filtering.*

## Variation of $\lambda$

Figure 21 displays susceptibility images of a middle slice of the phantom with varying cylinder diameters, with the cylinders orientated perpendicular to the main magnetic field, calculated with $\lambda = 1, 10, 100, 1000, 10\,000, 50\,000$. Clear differences in QSM image quality can be observed.

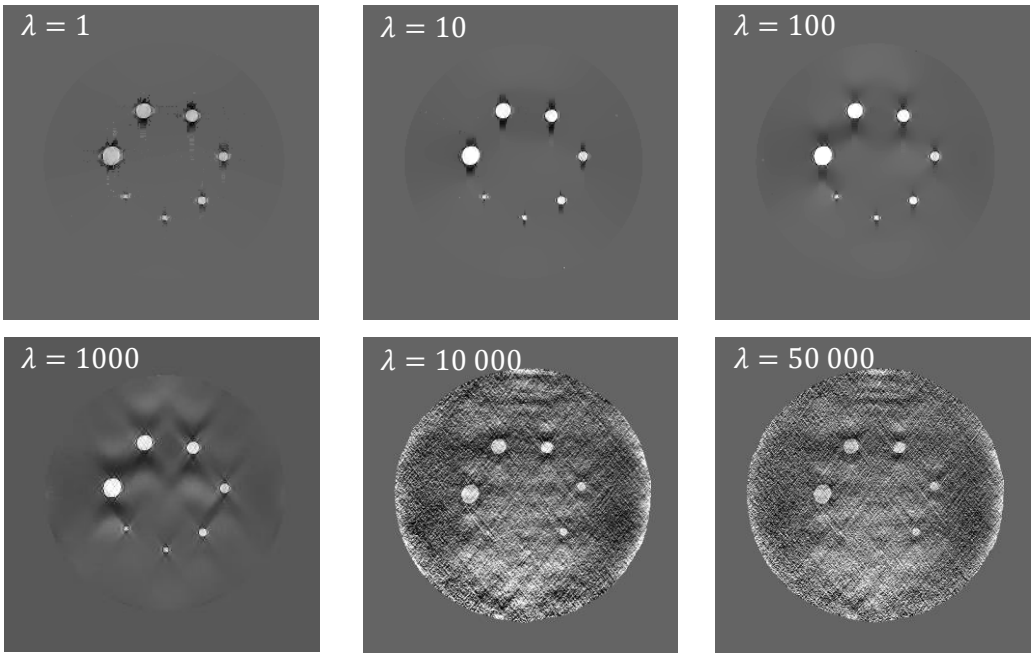


*Figure 21 Susceptibility images of the phantom with varying cylinder diameter, with the cylinders orientated perpendicular to the main magnetic field, calculated with different values of $\lambda$.*

Figure 22 shows how the calculated susceptibility depends numerically on the parameter $\lambda$, for the phantom with various angles. Even though the appearance of the QSM images are clearly affected by the choice of $\lambda$, the value of $\lambda$ seems to have a limited effect on the quantitative susceptibility values.

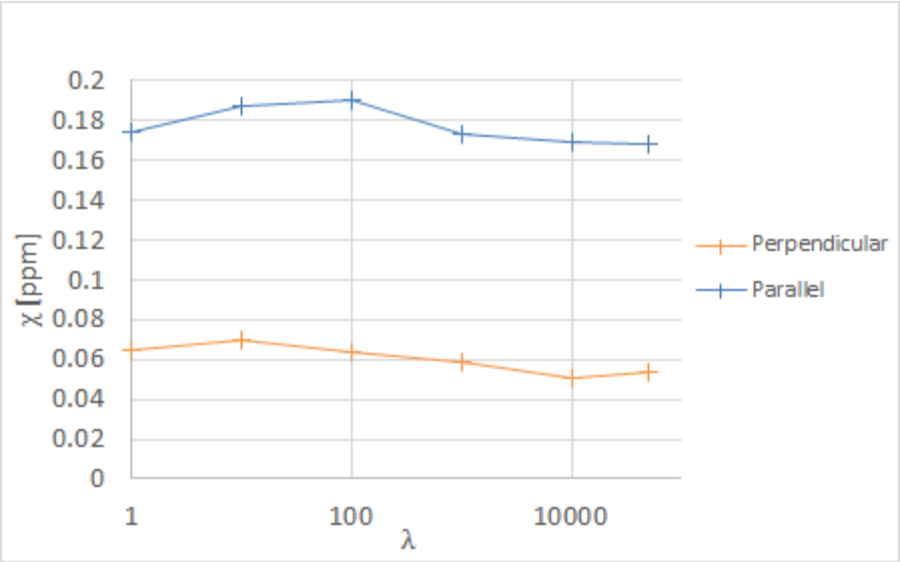


*Figure 22 The diagram shows the susceptibility in the perpendicular and the parallel cylinder calculated with different values of λ.*

*A* $\lambda$ of 1000 has been used as standard but for the measurement of the angle phantom the optimal $\lambda$ seems to be around 10. The effect on the final result however is small, se figure 23.

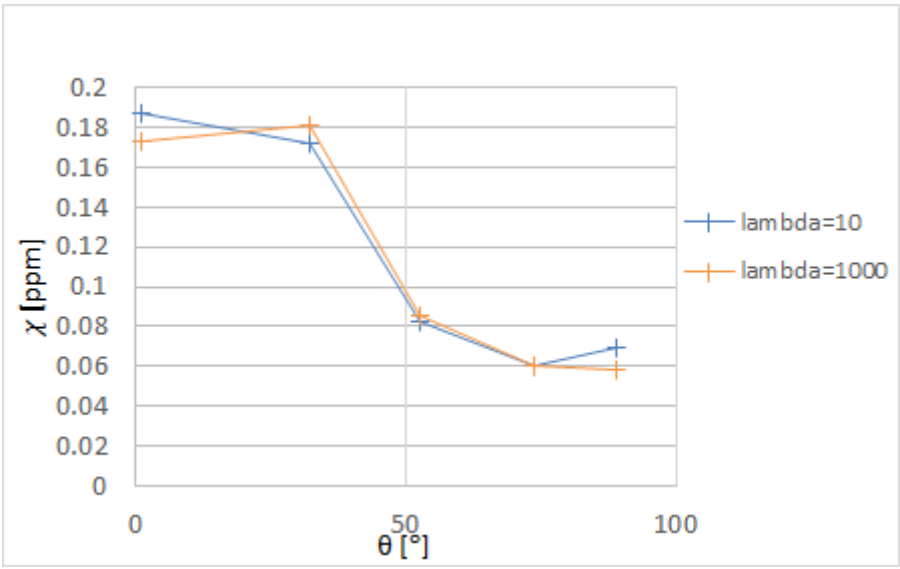


*Figure 23 Measured susceptibility in cylinders with varying angles, calculated using λ= 10 and 1000.*

## Zero padding

Figure 24 presents the result for the susceptibility calculated for the phantom with cylinders in various angles relative to the main magnetic field with and without zero padding. The zero padding does not seem to have any effect on the estimated absolute susceptibility values.

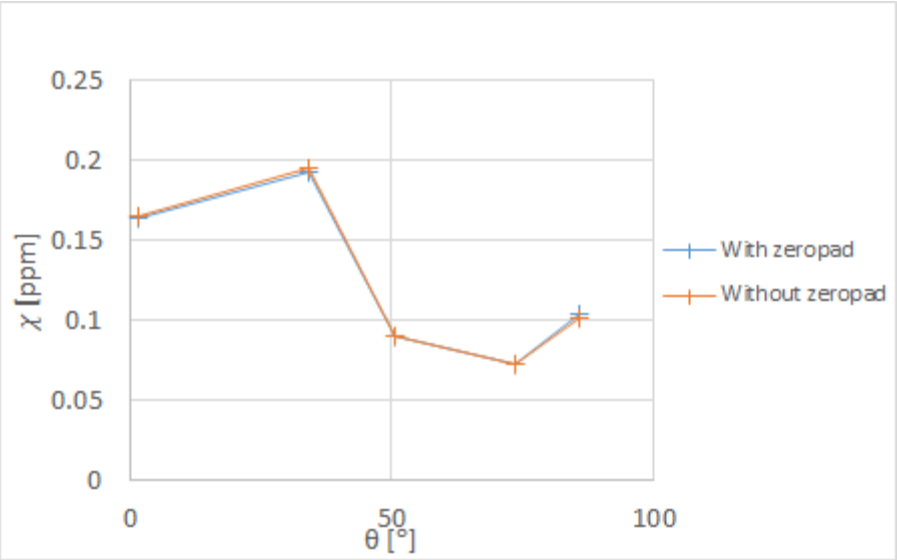


*Figure 24 Susceptibility in cylinders at different angles, calculated with and without using zero padding (200 zeros were added in all three directions).*

## Simulations

Simulated phase images and the corresponding artificial susceptibility maps, calculated from simulated phase data using the MEDI algorithm, are shown in Figures 25 and 26.

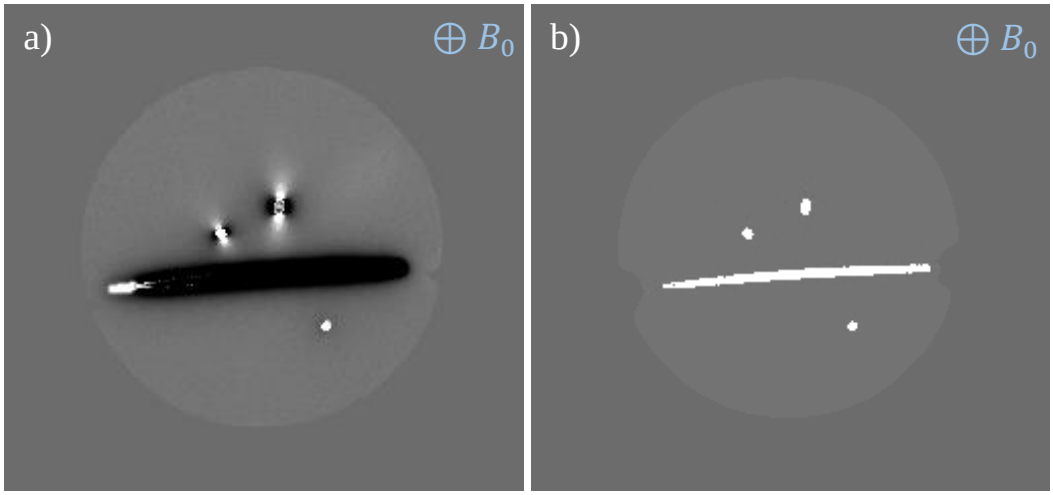


*Figure 25 (a) Simulated phase image and (b) the corresponding susceptibility image calculated with MEDI for slice 17 of 48 of the phantom with cylinders at different angles.*

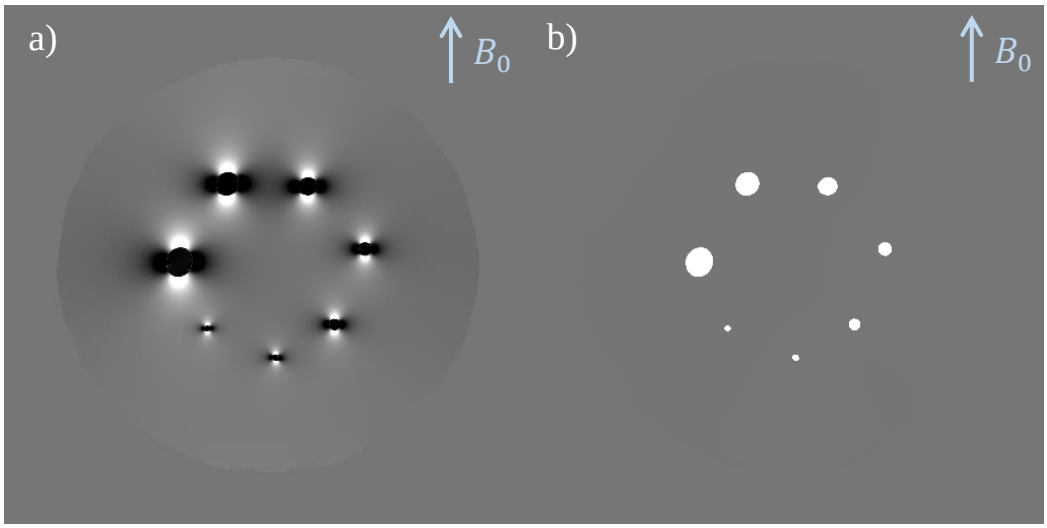


*Figure 26 (a) Simulated phase image and (b) the corresponding susceptibility image for slice 40 of 80 of the phantom with varying diameters. The images were simulated without noise for a matrix size of 512x512.*

Real and simulated phase images appeared visually similar, but in the simulated QSM images, no susceptibility dependence on the angle of the cylinder axis relative to the $B_0$-field was observed (see Figure 27). In the phantom with varying cylinder diameters, the simulated phase images resulted in susceptibility values that were in much better agreement with theory than the susceptibility values based on measured phase (see Figure 28). This could be compared to results from measured data in Figure 11(b) and 15.

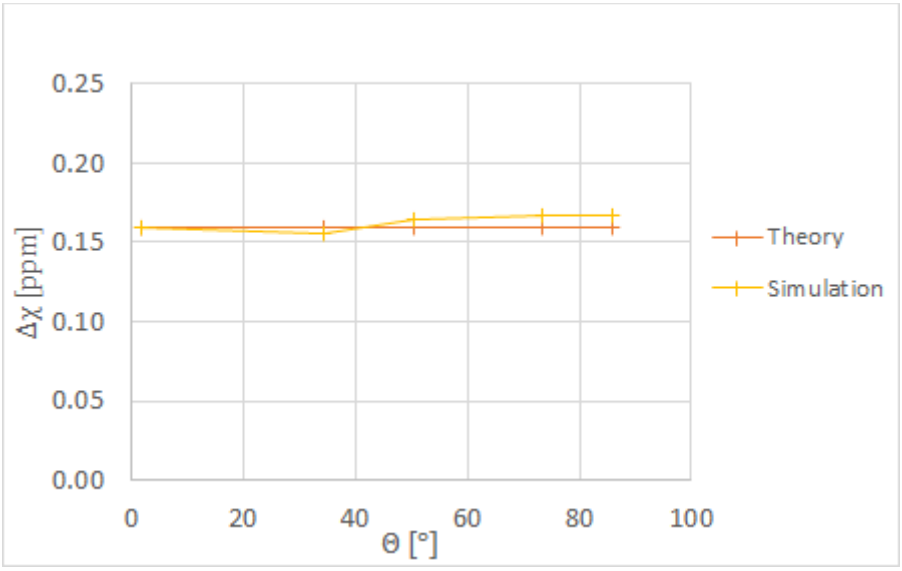


*Figure 27 Susceptibility measured in cylinders with different angles in simulated images.*

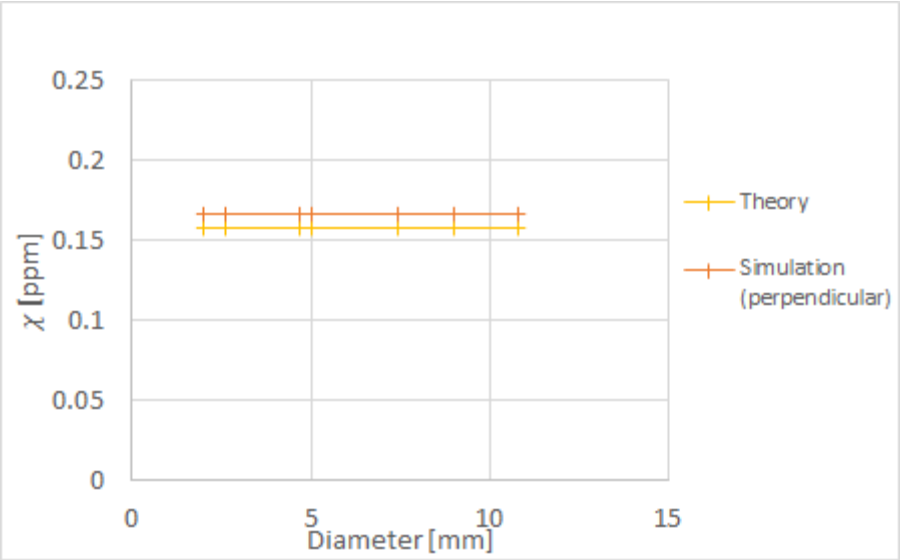


*Figure 28 The result of the susceptibility calculation for varying cylinder diameter for simulated phase data compared with the theoretical susceptibility.*

## Phase profiles

A profile was positioned through the 5 mm cylinder in measured and simulated phase images of the phantom with cylinders of varying diameters. Profiles were plotted both in-plane and along the slice direction as illustrated in Figure 29. The results are presented in Figures 30 and 31. Special attention was paid to the amplitude of the peaks at the cylinder edges; no marked difference in peak amplitude were seen between measured and simulated phase for the in-plane profile. However, in the slice direction the simulated peak phase was considerably higher than the measured phase.

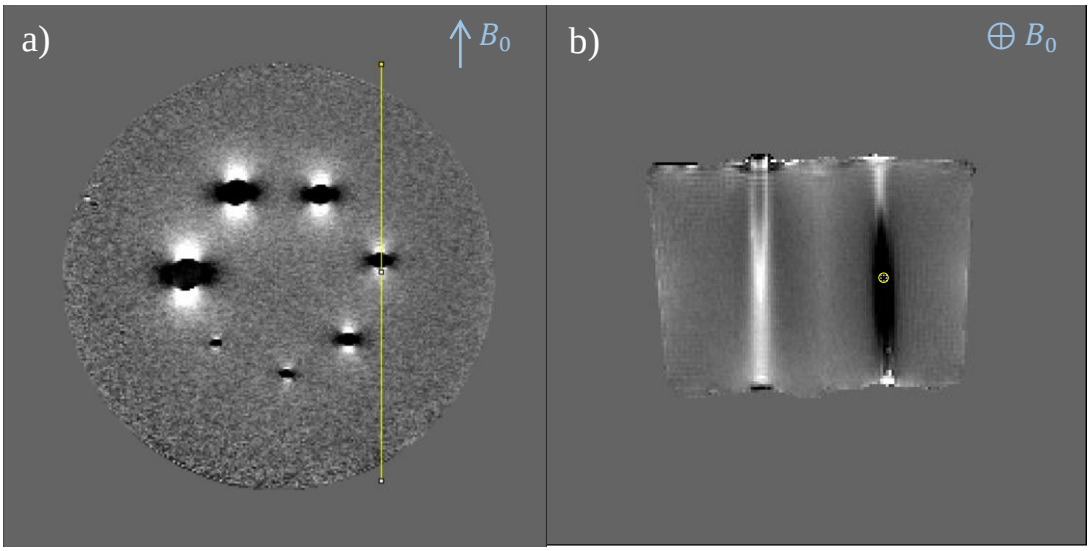


*Figure 29 A profile positioned through the 5 mm cylinder perpendicular to the field (a) in-plane and (b) along the slice direction. The measurements were identical, except for the use of different slice directions.*

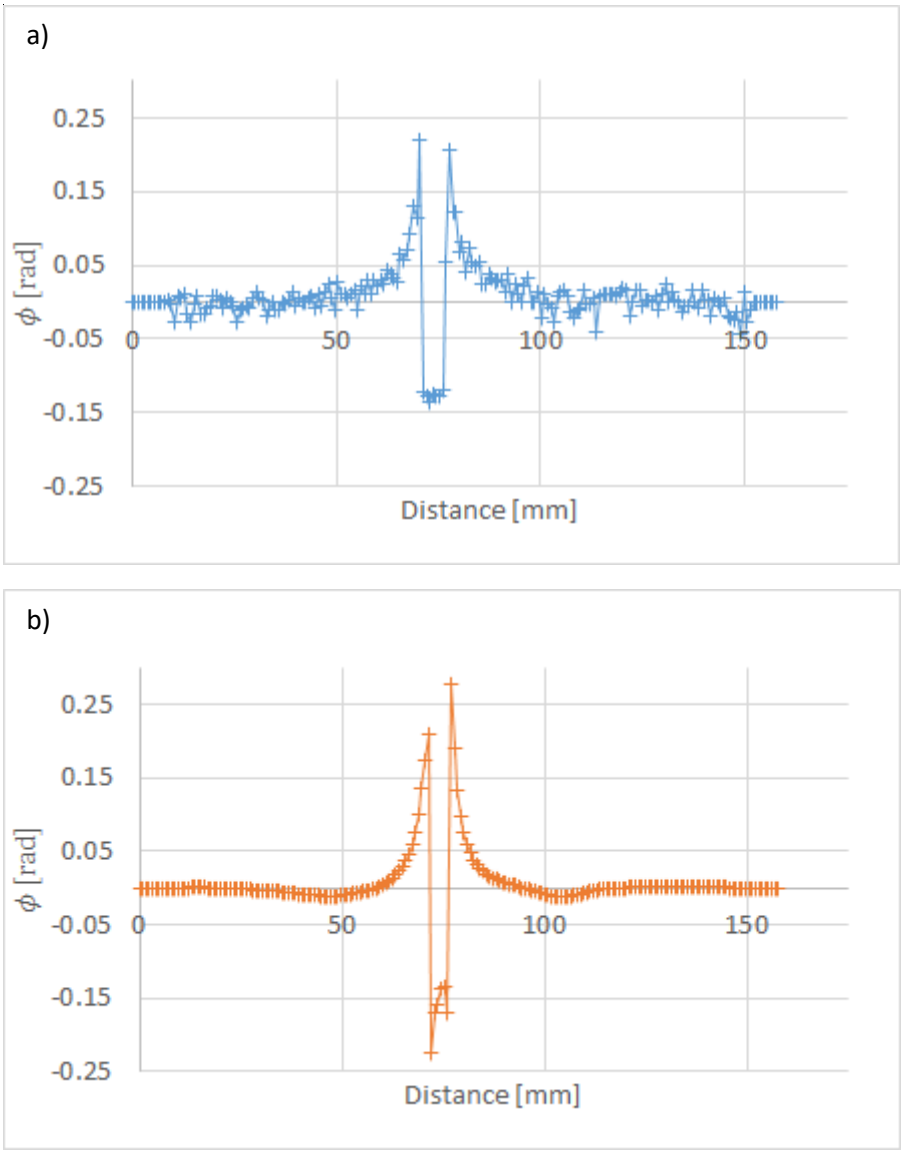


*Figure 30 Profile through the 5 mm cylinder in a slice in the middle of the volume of (a) measured and (b) simulated phase.*

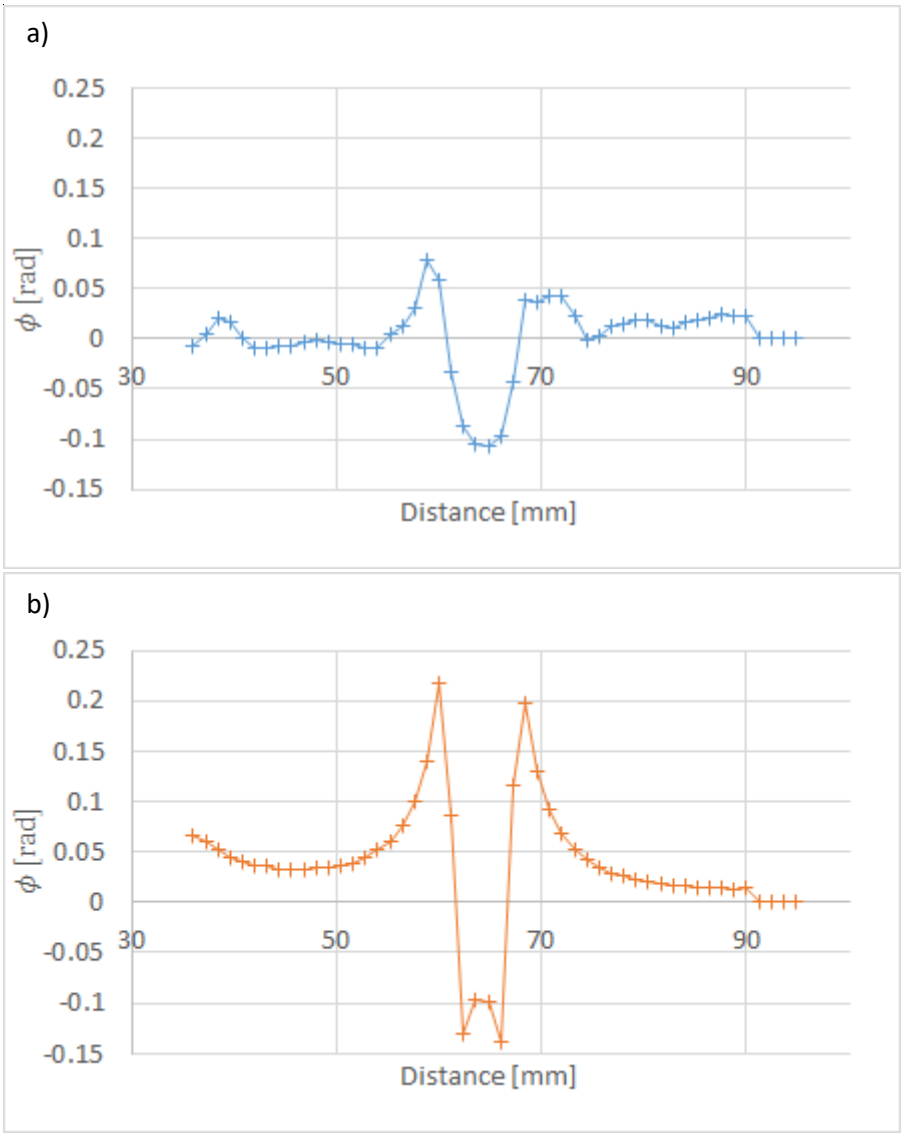


*Figure 31 Slice direction profile through the 5 mm cylinder. Comparison between (a) measured phase and (b) simulated phase.*

## In vivo measurement

Figure 32 shows phase and susceptibility images from the in vivo experiment. A distinct difference can be seen between phase-based and susceptibility-based information with regard to the blood vessel indicated by an arrow. The difference between phase and susceptibility is also illustrated in Figure 33, showing a profile that cuts the vessel at four locations.

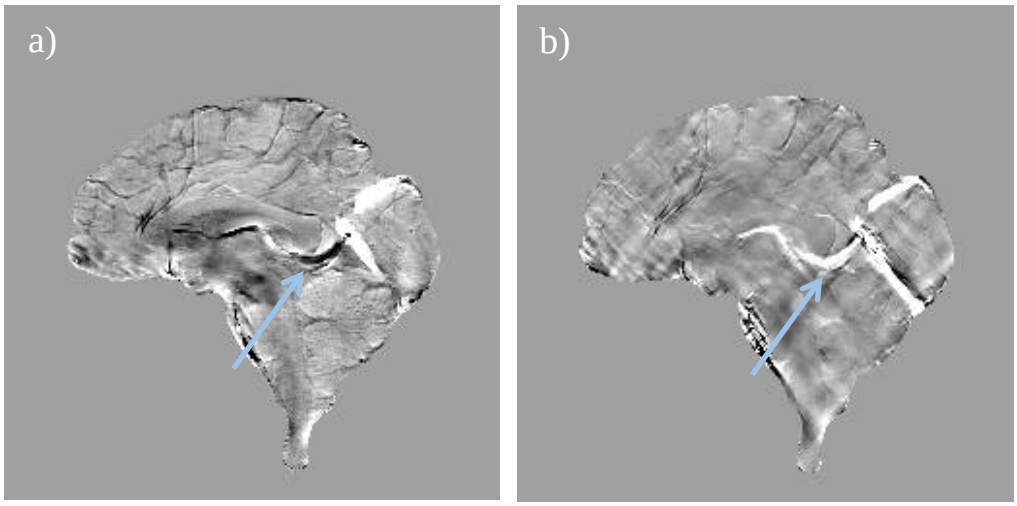


*Figure 32 (a) Sagittal phase image and (b) the corresponding susceptibility image of a human brain. The arrow indicates a blood vessel where a distinct difference in information can be seen between the phase image and the susceptibility image.*

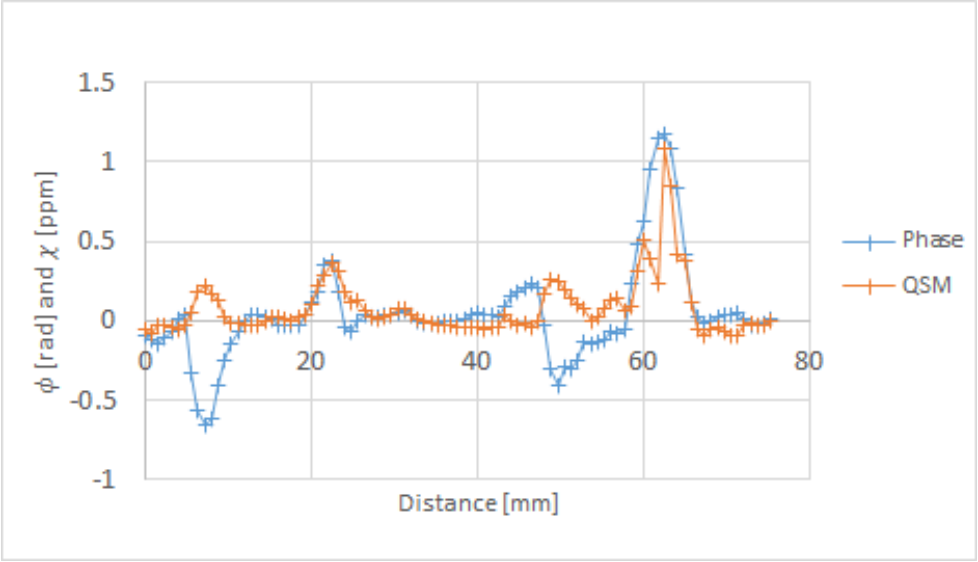


*Figure 33 A profile through a blood vessel in the phase and the QSM image.*

## Discussion

Cylindrical objects were used in this project due to their geometrical resemblance with blood vessels. The distinct angular dependence of the phase in a blood vessel (see Figure 32 a), made it likely to assume that cylinders could be a challenge for the QSM algorithm. Another advantage with the use of cylinders is that theoretical values for the local field can easily be calculated using Equations 6 and 7.

The initial presumption, that cylindrical objects could be problematic for the QSM algorithm, seemed valid based on the initial observation of the measured and theoretical data of the phase and susceptibility inside the cylinders at different angles relative to the main magnetic field (Figure 10). The simulated data, however, indicated that the QSM algorithm, in fact, generated magnetic susceptibility values that were very close to theory, even for angles larger than the magic angle. This can be seen both in Figures 27 and 28. Furthermore the simulated data did not show any dependence of estimated susceptibility on the diameter of the phantom, as can be seen in Figure 15.

The choice of the regularisation parameter $\lambda$ was expected to influence the susceptibility calculation because it has previously been shown that the error of the QSM method depends on the choice of $\lambda$ [12]. However, in the present study, the value of $\lambda$ seemed to influence primarily the image quality, but the absolute susceptibility estimates did not vary substantially.

From the measurements on cylinders filled with solutions of varying gadolinium concentrations, it was concluded that the estimated susceptibility depended linearly on the concentration of contrast agent, but the slope, both for the phase and for the susceptibility, did not agree with the theory. This implies that experimental data corresponded fairly well with theory for low concentrations of contrast agent, but for higher concentrations the deviation, in absolute terms, increased. This is consistent with previous studies since it has been shown that the error of the QSM calculation increases with increasing susceptibility [21].

For the 0.5 mM gadolinium solution, that was used also in the other phantom designs, the susceptibility value was reasonable but the error was not negligible. Comparing the results of Figures 11b) and 15 with Figure 13b) indicates that the deviation of the slope from theory (in Figure 13b)) corresponds well to the overestimation of the susceptibility for cylinders approximately parallel to the main magnetic field. One possible explanation is that the theoretical value for the molar susceptibility was not correct for the gadolinium compound used in this study, and that the theoretical slope was actually underestimated. Since the phase (in Figure 13a) is also biased by some unknown factor, leading to an overestimation compared with theory, it seems reasonable to conclude that the problem is not, at least not entirely, related to the susceptibility calculation but rather to the measurement or the reconstruction of the phase image.

The result from the use of simulated phase data confirmed that the problem of estimating the true susceptibility values for different angulations towards the main magnetic field was not inherent to the MEDI algorithm. The fact that the results were not much affected by the choice of $\lambda$ also suggests that the error arises from some other step in the procedure.

Therefore, three different filtering methods were applied to see if the problems arise due to the background phase removal. Although the results among different filtering methods were not identical, no filtering method returned a systematically more accurate result than the others. An attempt was also made to calculate the susceptibility without filtering. This resulted in images of poor quality, but the angular dependence of the susceptibility estimates remained.

As shown, the phase was measured correctly inside the cylinders but measured and simulated phase did not generate the same susceptibility results. Hence, a reasonable conclusion was that measured phase must differ from simulated phase outside the cylinder. The comparison of profiles between measured and simulated phase showed that the difference in phase between measurement and simulation occurred just outside the cylinder in the slice direction. Since the magnetization of the cylinder affects the phase not only inside the cylinder, but also in the area surrounding the cylinder, the background phase will influence the result of the susceptibility calculation. Hence, if the phase was not correctly measured in the background region, this constitutes a plausible explanation to why calculations failed to retrieve accurate values for the magnetic susceptibility.

Removing slices at the edges of the phase image stack before calculation resulted in images with less artefacts and a more uniform slice direction profile. This also suggests that phase estimates along the slice direction or at the edges of the imaged volume are influenced by factors which are still unknown. A larger volume coverage of the object resulted in susceptibility values closer to the theoretical value and in susceptibility images with a more uniform slice direction profile, similar to the case with exclusion of edge slices.

The spatial resolution also seemed to be of some importance for the accuracy of the estimated susceptibility since the estimated susceptibility values seems to vary between different voxel sizes.

For the smallest cylinders (diameters of 2 mm and 2.6 mm) some degree of partial volume effects can be expected, since the voxel size used was 1x1x2 $mm^3$, but even for the larger cylinders the estimates differed from the expected values. Figure 16 indicates that there is no dependence on the voxel size for the largest cylinder (10.8 mm in diameter), but for the 5 mm cylinder higher resolution resulted in a value closer to the theory. This implies, not surprisingly, that sufficient spatial resolution is needed to obtain optimal results. At a certain point, the combination of object size and spatial resolution gives sufficiently good measurement conditions, and the systematic error is minimal Obviously, for a smaller object a higher resolution is required to reach that point. However, to establish a clear relationship between image resolution and estimated susceptibility values, more data points would be needed.

Even though the estimated susceptibility was not always accurate in absolute terms, the contrast of the susceptibility images differed in general substantially from the corresponding phase images. This can be seen both in phantoms (see for example Figure 10 and 14) and in vivo (Figure 32). The unique contrast of QSM should in many cases be preferable compared with, for example, susceptibility weighted images (SWI) where the phase contrast is added to the magnitude image, retaining the geometric dependence of the phase.

In the sagittal image of a brain the distinct directional dependence of the phase of the blood vessel is clearly visible, as the phase shift goes from positive to negative when the blood vessel turns in a direction approximately perpendicular to the main magnetic field. This angular dependence along the vessel is not seen in the susceptibility image.

Finally, to obtain true quantitative susceptibility values more work is needed, because even if experimental phase data would become more accurate, the QSM results would still, in practice, be relative. The background in the phase images is set to zero, which will correspond to zero susceptibility, which is normally not the true value. In the phantoms, the true background value is known and thus the expected phase within the object can be calculated. In the human body, we do not have any such information. Hence, some reference region with known susceptibility is required in order to obtain the correct absolute level of susceptibility within the dataset.

For relative values it is still of importance to know under which conditions the measured values are reliable and when they are not. If the aim is to measure the susceptibility, for example, in a blood vessel, it might be advantageous to choose the slice direction along the direction of the vessel.

# Conclusions

The MEDI algorithm was demonstrated to be a quite stable method for QSM calculations. The choice of parameters and settings, for example, the regularization parameter $\lambda$, zero-padding and filtering method seemed not to have a large impact on the results. Most importantly, when applied to simulated phase maps, MEDI returned accurate susceptibility quantification also for challenging geometries.

Experimental susceptibility images were reasonable in appearance and differed substantially in contrast from the original phase images, implying that the QSM maps can be qualitatively useful, for example, at visual inspection.

For experimental phase data, the method did result in a linear relationship between susceptibility and concentration of contrast agent, but correct susceptibility was not obtained for cylindrical objects at an angle about or larger than the magic angle. The error seemed to originate from the measurement of the phase rather than from imperfections in the susceptibility calculation. Deviation from theory was observed primarily along the slice direction in the background of the measured phase images.

The experimental susceptibility results seemed to be somewhat more accurate for large objects or good spatial resolution, large volume coverage of the object and with the slice direction applied along the object of interest.

## Acknowledgements

I wish to express my gratitude to Emelie Lind and Ronnie Wirestam who started this project and without whom this work would not have been possible. Thank you for your unfailing support, great patience and good advice.

# References


1. M. Haacke, R. Brown, M. Thompson, and R. Venkatesan, *Magnetic Resonance Imaging: Physical Principles And Sequence Design - Chapter 25 Magnetic Properties of Tissues: Theory and Measurement*. 1999.

2. I. Lim et al. *Human brain atlas for automated region of interest selection in quantitative susceptibility mapping: application to determine iron content in deep gray matter structures.* Neuroimage. 2013;82:449-469

3. C. Stüber, D. Pitt and Y. Wang. *Iron in Multiple Sclerosis and Its Noninvasive Imaging with Quantitative Susceptibility Mapping.* International Journal of Molecular Sciences. 2016;17(1):100

4. J. Stankiewicz et al. *Iron in Chronic Brain Disorders: Imaging and Neurotherapeutic Implications.* Neurotherapeutics: the journal of the American Society for Experimental Neurotherapeutics. 2007;4(3):371-386.

5. J. H. Duyn and J. Schenck. *Contributions to magnetic susceptibility of brain tissue.* NMR in biomedicin 2016 DOI: 10.1002/nbm.3546

6. R. Wirestam. *Using contrast agents to obtain maps of regional perfusion and capillary wall permeability*. Imaging in Medicine 2012;4(4), 423–442

7. R. Cusack and N. Papadakis. *New robust 3-D phase unwrapping algorithms: application to magnetic field mapping and undistorting echoplanar images.* Neuroimage, 2002;16(3 Pt 1): 754–764.

8. T. Liu et al. *A novel background field removal method for MRI using projection onto dipole fields (PDF).* NMR in Biomedicin. 2011;24: 1129–1136

9. L. de Rochefort et al. *Quantitative susceptibility map reconstruction from MR phase data using bayesian regularization: validation and application to brain imaging.* Magnetic Resonance in Medicine 2010;63(1):194-206

10. D. Zhou et al. *Background field removal by solving the Laplacian boundary value problem.* NMR in biomedicine 2014;27(3):312-9

11. H. Sun and AH. Wilman. *Background field removal using spherical mean value filtering and Tikhonov regularization.* Medical Resonance in Medicine 2014;71(3):1151-7

12. J. Liu et al. *Morphology enabled dipole inversion for quantitative susceptibility mapping using structural consistency between the magnitude image and the susceptibility map.* Neuroimage 2012;59(3):2560-8.

13. T. Liu et al. *Nonlinear formulation of the magnetic field to source relationship for robust quantitative susceptibility mapping.* Magnetic Resonance in Medicine 2013;69(2):467-76

14. T. Liu et al. *Morphology enabled dipole inversion (MEDI) from a single-angle acquisition: comparison with COSMOS in human brain imaging.* Magnetic Resonance in Medicine 2011;66(3):777-83

15. JO. Christoffersson, LE. Olsson and S. Sjöberg. *Nickel-doped agarose gel phantoms in MR imaging.* Acta Radiologica. 1991;32(5):426-31

16. J.A. Pople, W.G. Schneider and H.J. Bernstein. *High-resolution Nuclear Magnetic Resonance.* New York: McGraw-Hill Book Company, Inc. 1959

17. C. Bakker and R. Roos. *Concerning the Preparation and Use of Substances With a Magnetic Susceptibility Equal to the Magnetic Susceptibility of Air.* Magnetic Resonance in Medicine 2006;56(5):1107-1113

18. W.M. Haynes. CRC Handbook of *Chemistry and Physics, 93rd Edition -Section 4 Properties of the elements and inorganic compounds.* 2012

19. L. Rochefort et al. *Quantitative MR Susceptibility Mapping Using Piece Wise Constant Regularized Inversion of the Magnetic Field.* Magnetic Resonance in Medicine 2008;60:1003–1009

20. Cornell MRI Research Group 2013 *http://weill.cornell.edu/mri/pages/qsm.html*

21. A. Karsa et al. *The Effect of Large Slice Thickness and Spacing and Low Coverage on the Accuracy of Susceptibility Mapping.* Proceedings of the 24th Annual Meeting of ISMRM, Singapore, 2016. p 1555